

PAPER • OPEN ACCESS

Spatial self-organization of macroscopic quantum states of exciton-polaritons in acoustic lattices

To cite this article: J V T Buller *et al* 2016 *New J. Phys.* **18** 073002

View the [article online](#) for updates and enhancements.

Related content

- [Quantum fluids of light in acoustic lattices](#)
E A Cerda-Méndez, D N Krizhanovskii, M S Skolnick *et al.*
- [Superfluidity in polariton condensates](#)
A Amo, J Lefrère, C Adrados *et al.*
- [A polariton condensate in a photonic crystal potential landscape](#)
Karol Winkler, Julian Fischer, Anne Schade *et al.*

Recent citations

- [Quantum fluids of light in acoustic lattices](#)
E A Cerda-Méndez *et al*



PAPER

Spatial self-organization of macroscopic quantum states of exciton-polaritons in acoustic lattices

OPEN ACCESS

RECEIVED

8 December 2015

REVISED

27 May 2016

ACCEPTED FOR PUBLICATION

6 June 2016

PUBLISHED

1 July 2016

Original content from this work may be used under the terms of the [Creative Commons Attribution 3.0 licence](#).

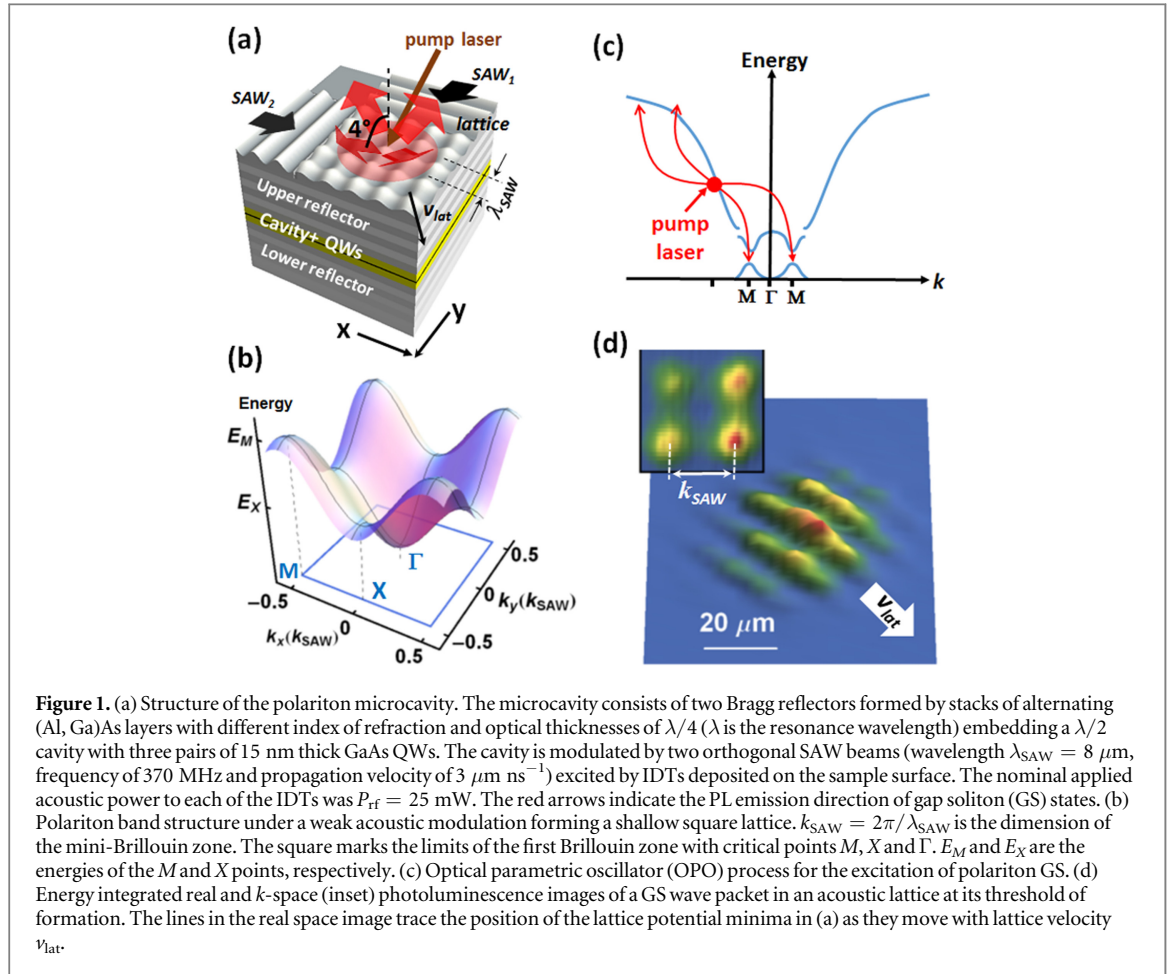
Any further distribution of this work must maintain attribution to the author(s) and the title of the work, journal citation and DOI.

J V T Buller¹, E A Cerda-Méndez^{2,4}, R E Balderas-Navarro², K Biermann¹ and P V Santos¹¹ Paul-Drude-Institut für Festkörperelektronik, Hausvogteiplatz 05-7, D-10117 Berlin, Germany² Instituto de Investigación en Comunicación Óptica, Universidad Autónoma de San Luis Potosí, Av. Karakorum 1470, Lomas 4ª Secc, 78210, San Luis Potosí, México³ Instituto de Física Universidad Autónoma de San Luis Potosí, Av. Manuel Nava #6, Zona Universitaria, C.P. 78290 San Luis Potosí, México⁴ Author to whom any correspondence should be addressed.E-mail: ecerda@cactus.iico.uaslp.mx**Keywords:** semiconductor microcavities, surface acoustic waves, exciton-polaritons, solitonsSupplementary material for this article is available [online](#)**Abstract**

Exciton-polariton systems can sustain macroscopic quantum states (MQSs) under a periodic potential modulation. In this paper, we investigate the structure of these states in acoustic square lattices by probing their wave functions in real and momentum spaces using spectral tomography. We show that the polariton MQSs, when excited by a Gaussian laser beam, self-organize in a concentric structure, consisting of a single, two-dimensional gap-soliton (GS) state surrounded by one dimensional (1D) MQSs with lower energy. The latter form at hyperbolic points of the modulated polariton dispersion. While the size of the GS tends to saturate with increasing particle density, the emission region of the surrounding 1D states increases. The existence of these MQSs in acoustic lattices is quantitatively supported by a theoretical model based on the variational solution of the Gross-Pitaevskii equation. The formation of the 1D states in a ring around the central GS is attributed to the energy gradient in this region, which reduces the overall symmetry of the lattice. The results broaden the experimental understanding of self-localized polariton states, which may prove relevant for functionalities exploiting solitonic objects.

1. Introduction

The manipulation of macroscopic quantum states (MQS), systems where a collection of particles share a single macroscopic wave function, is a fascinating topic that has been investigated in diverse research fields [1, 2]. The possibility to engineer artificial periodic potentials to shape the properties of a MQS has allowed the simulation of solid-state quantum phase-transitions [3], the implementation of quantum computation protocols [4] and the exploration of the cross-over of MQS physics with nonlinear optics concepts [5]. Notable examples of MQS systems are atomic Bose-Einstein condensates (BECs) in optical and/or magnetic traps and supercurrents in superconducting circuits. Another type of MQS exists in semiconductor planar microcavities (MC) [6, 7], where, in contrast to atoms in BECs or Cooper pairs in superconductors, the components are photonic states dressed by excitons called exciton-polaritons. Exciton-polaritons are bosonic light-matter quasi-particles that form when photons couple strongly with quantum-well (QW) excitons in a semiconductor MC. While the inter-excitonic interactions provide an optical nonlinearity which is several orders of magnitude stronger than in purely photonic systems, the small mass arising from the photonic component gives polaritons a de Broglie wavelength of a few micrometres. The latter enables them to generate MQSs at lower densities and higher temperatures (on the order of a few kelvin) than in atomic systems as well as to be coherently manipulated by micrometric potentials [8–15]. Of particular interest are tuneable modulation schemes, which can produce potentials for polaritons analogue to optical lattices for cold atoms. Such potentials may be provided by the



strain field of surface acoustic waves (SAWs) propagating on the MC surface (figure 1(a)). The SAW strain modulates the energies of the excitonic and photonic polariton components, resulting in the formation of a lattice with a periodicity given by the SAW wavelength [16].

The polariton nonlinearity may give rise to the formation of states with interesting properties in such lattices. In a former report [13], we have demonstrated that polariton MQSs support self-localized modes within the gaps of the lattice band structure (gap solitons (GSs)). Similar observations were also reported for modulated polariton wires [12]. The GS modes originate from the interplay between repulsive inter-particle interactions and attractive forces at critical points of negative effective mass of the lattice band structure.

One interesting question that we address is whether a single or multiple GS states form within the laser excitation spot. In a previous report, we have observed that the total diameter ϕ_{PL} of the photoluminescence (PL) emission area of MQSs in an acoustic lattice exceeds the characteristic length $\ell = 2\pi/\Delta k$, where Δk is the full-width at half-maximum of the k -space emission pattern. Such characteristic length is defined assuming a Gaussian shape for the intensity spatial profiles of the square modulus of the GS wave function as well as of the k -space emission peaks (we show in the supplementary material that this assumption applies in the present case; under this conditions, the Heisenberg-like relationship between position and momentum becomes an equality). The discrepancy between the total diameter ϕ_{PL} and the parameter ℓ could indicate a multiphase behaviour. Here, we use a spectrographic tomography technique [17] to access detailed information about the spatial structure of MQSs in two-dimensional (2D) acoustic lattices. We show that these MQSs have a rich structure consisting of three main components. The main one is a single, 2D GS mode [13] spatially located close to the centre of the excitation laser spot. This mode consists of an admixture of states around the M -points of the reciprocal square lattice (see figure 1(b)). The size of the GS wave packet increases with the excitation density up to a certain value, and then remains constant for higher ones. The GS dominates the emission over a wide range of optical excitation powers and coexists with other two sets of spatial modes arranged in concentric rings around it. The first surrounding ring is composed of an ensemble of one dimensional (1D) MQSs that form around the hyperbolic X -points of the polariton dispersion. The second ring consists of an incoherent gas of polaritons surrounding the two former ones. This spatial arrangement is determined by polariton interactions and by the size and intensity profile of the laser spot. Indeed, in the energy-integrated images reported in [13], all

these modes are superimposed in the images of the real space emission, thus leading to an apparent inconsistency between the characteristic length ℓ and the observed wave packet size ϕ_{PL} . Finally, we directly probe the intrinsic size of the GS, which is determined by the polariton interactions and effective mass.

This paper is organized as follows. Section 2 describes the structure of the studied sample and the spectrographic tomography technique used in the investigations. In section 3, we present experimental results for the structure of the MQSs recorded for different laser excitation conditions. In section 4, we discuss in detail how the experimental findings can be related to polariton MQSs with different symmetries. The latter are further supported by the theoretical model based on a variational solution of the Gross–Pitaevskii equation (GPE) presented in section 4, which describes quantitatively the experimental observations. Finally, section 5 summarizes the concluding remarks.

2. Methods

The experiments were carried out on an (Al, Ga)As-based $\lambda/2$ optical resonator ($\lambda = 808$ nm is the wavelength of the confined optical mode) consisting of six 15 nm thick GaAs-QWs sandwiched between two distributed Bragg reflectors (see figure 1(a)). Details of the sample structure are described in the figure caption and in [13, 16]. All measurements were performed at $T = 8$ K. On top of the sample structure a $170 \times 170 \mu\text{m}^2$ sinusoidal square lattice is created by the interference of two orthogonal SAWs [18], each with an acoustic wavelength $\lambda_{\text{SAW}} = 8 \mu\text{m}$ (see figure 1(a)). The SAWs propagate along two $\langle 100 \rangle$ surface directions and are generated by interdigital transducers (IDTs) placed on thin piezoelectric ZnO islands.

The polaritons MQSs were excited by a single-mode, continuous-wave, Gaussian pump laser in an optical parametric oscillator (OPO) geometry. For that purpose, the laser energy was tuned to 1.5353 meV and its angle of incidence to 13° in order to inject photons in resonance with the polariton dispersion. Under the SAW potential, the polaritons injected by the pump laser scatter not into the lower energy state at $k = 0$, but into the critical points at the borders of the 1st Brillouin Zone (see figure 1(c)) [13]. The laser power will be specified in terms of either the total laser power P_L or in terms of the optical power density defined as the ratio between P_L and the area enclosed by the laser spot at full width at half maximum (FWHM) of power intensity.

The polariton PL collected from the sample top surface was imaged with either spatial or angular (i.e. planar momentum) resolution onto a charged coupled device (CCD) at the output port of a spectrometer. When the input slit of the spectrometer (vertically (y -) oriented in figure 1(a)) is fully open and its dispersion grating set to zero-order diffraction, the CCD detector records an energy-integrated real space image of the PL (i.e., figure 1(d)). The k -space images are obtained by measuring the PL with angle resolution, since the emission angle θ is directly related to the planar momentum by $\mathbf{k}_{\parallel} = \mathbf{k} \sin(\theta)$, where $k = 2\pi/\lambda_{\text{PL}}$ is the photon wave vector (λ_{PL} is the PL wavelength).

If the spectrograph slits are closed and its grating angle set to first-order diffraction, the previous procedure yields spectral information of a cross-section of the real or momentum-space image defined by the slit (with spectral resolution of $60 \mu\text{eV}$). Full real and momentum space tomograms have been acquired by using a lens to shift the PL images across the slit and, in this way, to reconstruct the complete image with spectral resolution [17]. This procedure yields thus a six-dimensional matrix of the PL emission (x, y, k_x, k_y , energy, PL intensity).

3. Experimental results

3.1. Modulation of polaritons by SAWs

The long de Broglie wavelength of the polaritons enables the formation of tuneable lattices via the modulation by SAW beams propagating on the microcavity structure, as illustrated in figure 1(a). The SAW strain field modulates both the MC optical resonance energy and the band gap of the embedded QWs [16], resulting in the formation of a lattice potential with periodicity given by the SAW wavelength. As for optical lattices of cold atoms, the main advantage of the acoustic modulation is the tuneability arising from the fact that the lattice amplitude Φ_{SAW} can be controlled by the radio-frequency power P_{rf} applied to excite the SAWs ($\Phi_{\text{SAW}} \propto \sqrt{P_{\text{rf}}}$).

The acoustic modulation by orthogonal SAWs creates a square lattice potential with mini-Brillouin-Zones (MBZs) of dimension $k_{\text{SAW}} = 2\pi/\lambda_{\text{SAW}}$ separated by energy gaps. The lowest dispersion branch in a shallow lattice (i.e., created with small SAW amplitudes) is illustrated in figure 1(b). Note that the curvature of the dispersion, which is convex at Γ , inverts at X and M , indicating that these states have a negative effective mass. While M has a negative effective mass along both $M \rightarrow \Gamma$ and $M \rightarrow X$, X is a saddle point with positive mass m_p along $X \rightarrow M$ and negative mass along $X \rightarrow \Gamma$.

As described in the Methods section, the polariton MQS forms through an OPO process by resonantly pumping the polariton dispersion close to its inflection point. At high particle densities, the polariton–polariton repulsive interactions shift the dispersion towards high energies. By positively detuning the laser energy from the

lower polariton dispersion by a small amount (a few hundred μeV) it is possible to inject enough polaritons until the ‘blue-shifted’ dispersion matches the laser energy at high excitation power. When enough polaritons are injected, and in the absence of acoustic modulation, the scattering from the laser excitation state at \mathbf{k}_p (i.e. the pump state) becomes stimulated into two energy- and momentum-conjugated states of the dispersion: one with momentum $\mathbf{k}_s = 0$ and energy $E_s = 0$ (we define zero energy at $k_{\parallel} = 0$, this is, the bottom of the dispersion) and another at $\mathbf{k}_i = 2\mathbf{k}_p$ and $E_i = 2E_p$. These states are called the signal and the idler, respectively. The signal thus gives rise to the emission of a single beam propagating in the direction normal to the sample surface. The idler manifests as a second, weaker beam which is oblique to the sample surface with an angle approximately twice that of the pump laser. In our experiments, the idler beam is blocked by the cryogenic apparatus, as the numerical aperture of the optical windows is not big enough to let it out. In the absence of the acoustic modulation, the ‘signal’ PL is emitted in the direction normal to the surface. In a shallow lattice, in contrast, there are four ‘signals’ at the M points of the first MBZ of the modulated dispersion, and thus, the emission is composed of four beams emanating at an angle of 4° with respect to the surface normal, as illustrated in figure 1(a) and experimentally shown in the inset of figure 1(d). The OPO process is thus modified as shown in figure 1(c): the pump state scatters now into four signals around $\mathbf{k}_{\parallel} = 0$ and their corresponding conjugate idlers around $2\mathbf{k}_p$. Due to the correspondence between the angle of emission and the k -space coordinates, this indicates the formation of a GS at the negative effective mass M -points [13]. This special scattering configuration is attributed to the fact that the negative effective mass favors the preferential accumulation of particles at M , thus triggering an OPO process involving states at M rather than at Γ . In fact, the threshold for GS formation is substantially lower than the one for a conventional MQP in the absence of an acoustic modulation, as demonstrated in [13].

As mentioned above, the GS characteristic length ℓ is estimated from the FWHM (Δk) of the k -space images (see inset of figure 1(d)) according to $\ell = 2\pi/\Delta k$, and is compared to the size of the wave packet in real space. Figure 1(d) displays energy-integrated real- and k -space (inset) PL images of the MQS. The value of P_L is in this case slightly above the MQS excitation threshold P_{th} . Under this condition, the diameter of the real-space emission region ϕ_{PL} is close to $\ell = 25 \mu\text{m}$ obtained from the k -space image, as reported in [13]. The diagonal lines on the image trace the path of maxima of the MQS wave function, which moves with the lattice along the lattice diagonal with a velocity $v_{\text{lat}} = \sqrt{2} v_{\text{SAW}}$ (v_{SAW} is the phase velocity of each acoustic beam).

When the optical excitation power increases above the threshold value P_{th} , ϕ_{PL} grows at a much faster rate than ℓ determined from the corresponding k -space images. This behaviour is illustrated by the energy-integrated PL images (in false colour intensity scale) in the top row of figure 2. The latter were recorded with increasing optical powers from left to right (the left-most images for $P_L = P_{\text{th}}$ are the same as in figure 1(d)) with a laser spot of diameter $\phi_L = 70 \mu\text{m}$. Figure 3(a) displays the power density dependencies of ℓ and ϕ_{PL} (filled squares and dots, respectively) measured from these images. Interestingly, while ϕ_{PL} almost triples as P_L increases from $2P_{\text{th}}$ to $8P_{\text{th}}$, ℓ increases by less than 10%. For higher power densities, both ϕ_{PL} and ℓ tend to saturation. The main modification in the k -space images at high pump levels is an enhancement of the emission along the $X \rightarrow M$ directions of the MBZ (right top images of figure 2).

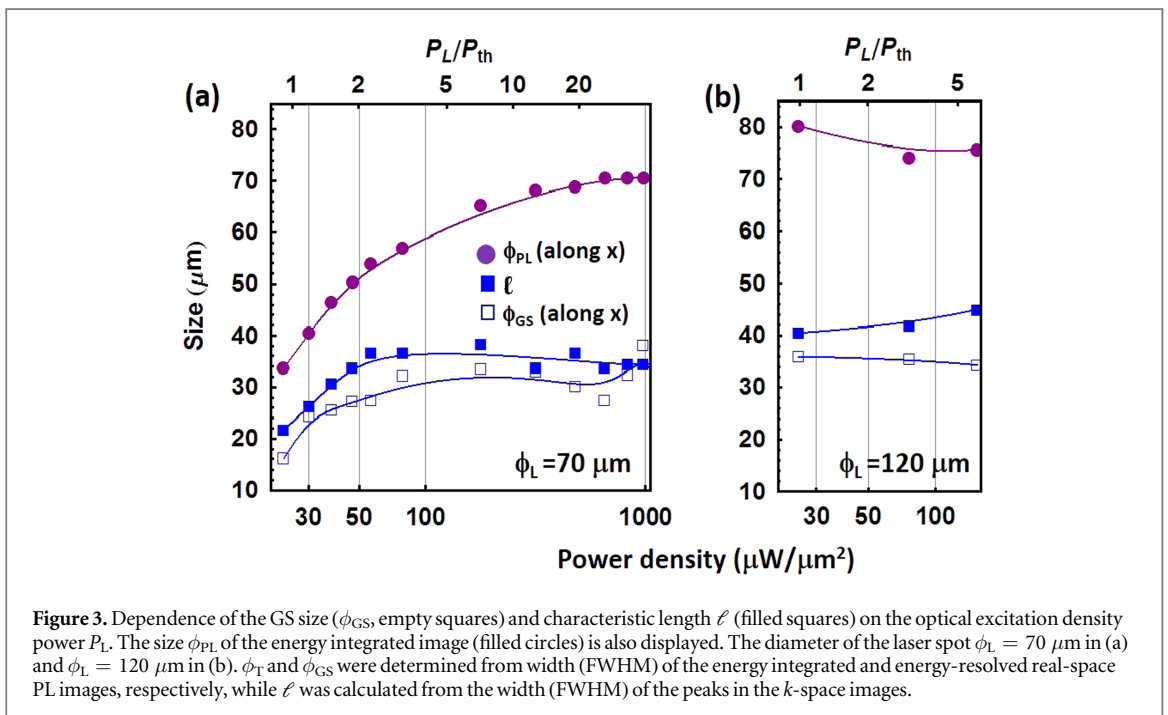
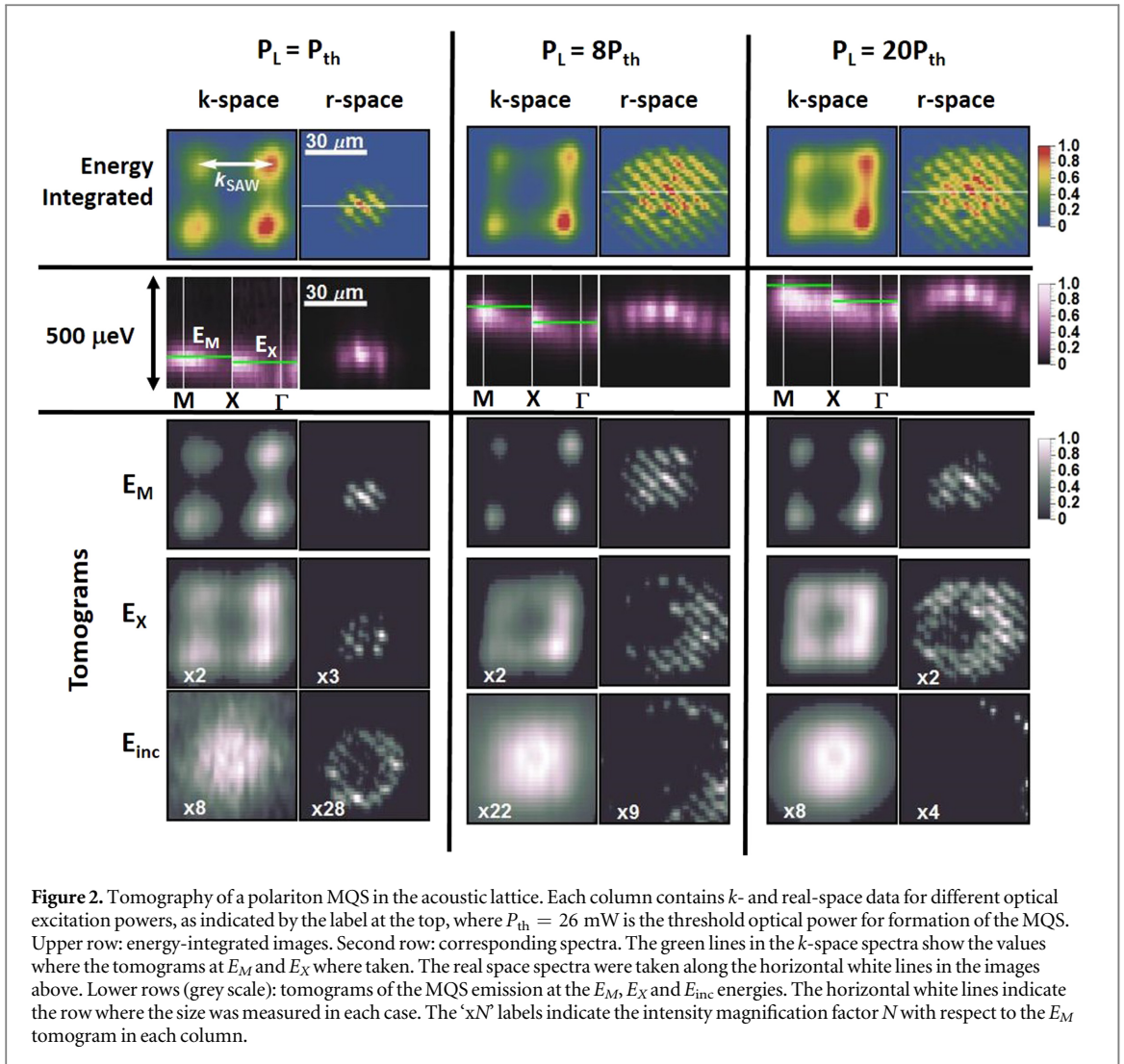
Large differences between ℓ and ϕ_{PL} have also been observed under excitation with a larger laser spot ($\phi_L = 120 \mu\text{m}$, filled squares and dots, respectively, in figure 3(b)). The threshold (corresponding to the power density for the first point in the curve) is, however, very similar to the one obtained for the $\phi_L = 70 \mu\text{m}$ spot. Furthermore, it is interesting to note that, under this large spot, ℓ is essentially independent of the excitation density and has a value close to the one measured for power densities $> 50 \mu\text{W} \mu\text{m}^{-2}$ for the small (i.e., $\phi_L = 70 \mu\text{m}$) laser spot (see figure 3(a)).

3.2. Tomography results

The differences between the ϕ_{PL} and ℓ obtained from energy-integrated images for excitation powers above P_{th} raise the question of whether the size of the GS increases with excitation intensity or whether multiple GSs with different symmetries and energies form within the illumination spot.

The plots on the second row of figure 2 display spectrally resolved cross-sections recorded along the horizontal lines superimposed on the real-space images of the upper row. Note that the emission energy actually varies across the spot. The corresponding k -space spectra show that the emission energy E_X from the X points is slightly red-shifted with respect to the emission energy E_M of the M points. The rigid spectral blue-shift increase with P_L is attributed to the polariton–polariton repulsive interactions, which renormalize the lattice dispersion [19].

In order to address the relationship between ϕ_{PL} and ℓ , we have recorded spectrally resolved PL images (PL tomograms) to access the internal structure of the MQS. Results obtained using a laser excitation spot of $\phi_L = 70 \mu\text{m}$ are shown in the third and fourth rows of figure 2 (in monochromatic intensity scale). In each case, the energies E_M and E_X are marked by the green lines on the plots of the spectra in the second row. The last row



shows, for completeness, maps acquired at a lower energy $E_{\text{inc}} = E_M - 200$ meV, which are associated with the weak emission from incoherent polariton states.

The tomograms show regions of different behaviour depending on the excitation density:

- Close to the condensation threshold (i.e., for $P_L = P_{\text{th}}$) the emission pattern is dominated by the 2D GS with energy E_M . It consists of a spot with a diameter of $23 \mu\text{m}$, which is close to the one obtained from energy integrated measurements (first row of figure 2). The energy difference $E_M - E_X$ between the GS and the surrounding states at E_X is small compared with the spectral resolution: a careful analysis of the images show, however, that the emission from the states at E_X comes predominantly from a ring around the central GS emission. Both emission regions are surrounded by a weak background with energy E_{inc} .
- At moderate excitation levels (P_L up to $8P_{\text{th}}$, middle column of figure 2), the distinction between the GS and X states becomes clear. As in the previous case, most of the emission is dominated by the GS state at the centre of the excitation spot, which has now expanded to a diameter of $35 \mu\text{m}$. This spatial extension is close to the value of ℓ obtained from the corresponding k -space map, thus indicating the presence of a single GS state. The GS spot is now, however, surrounded by a ring-shaped region with lower energy of emission E_X . The related k -space map shows that it consists of MQSs formed along the $X \rightarrow M$ directions of the MBZ. Applying the same spatial analysis to these k -space maps, we see that these $X \rightarrow M$ states have thus different values of ℓ along two perpendicular directions: they are confined within one λ_{SAW} in one direction, and spread over approximately two to three λ_{SAW} over the other one. Since these dimensions are smaller than the observed dimensions of the ring emission area, we conclude that several 1D MPQs oriented along x and y coexist in this region. Finally, the real-space spectra in the second row of figure 2 show that the $X \rightarrow M$ emission stems from regions with a large gradient in excitation intensity (and in emission energy) on the flanks of the laser beam.
- At the highest P_L value (see plots for $P_L = 20P_{\text{th}}$ at the rightmost column in figure 2), the size and the characteristic length ℓ of the 2D GS state at the centre of the laser spot remain essentially unchanged when compared to the results for $P_L = 8P_{\text{th}}$. The k -space map at E_X shows, however, that the emission from the $M \rightarrow X$ directions increases significantly and, from the corresponding real space image, we observe that it now completely surrounds the central GS state. Furthermore, the spectrum in the second row shows that the $M \rightarrow X$ emission band becomes now completely flat with an emission energy close to the GS.

4. Discussion

The tomography studies reveal the rich structure of polariton MQSs excited in the acoustic lattice, which consists of three modes of different symmetries and spatial distributions. In particular, they allow us to clarify the relationship between the ℓ parameter and the real-space diameter ϕ_{GS} (open squares, measured along the white lines of the E_M panels of figure 2) of the GS wave packets. Figure 3(a) shows that the ϕ_{GS} values (open squares) agree very well with the value of ℓ determined from the k -space maps. Both values are, however, much smaller than the diameter of the real-space spots determined from energy-integrated images (ϕ_{PL} , full dots).

The diameter ϕ_{GS} and the characteristic length ℓ of the GS wave packet increase from $23 \mu\text{m}$ at the threshold power density to $30 \mu\text{m}$ at $50 \mu\text{W} \mu\text{m}^{-2}$ (empty and filled squares in figure 3). Interestingly, above this value, the GS size stops expanding at a value $\phi_{\text{GS}} \cong \ell \cong 35 \mu\text{m}$. For the MQSs excited with a larger laser spot ($\phi_L = 120 \mu\text{m}$ wide, see open squares in figure 3(b)) the corresponding values for ϕ_{PL} and ℓ are roughly constant over the whole range of excitation powers and only slightly larger than the saturation value obtained for the small spot. For both spot sizes, $\phi_{\text{PL}} \cong \ell$ over the whole range of excitation powers, thus indicating that only a single 2D GS forms within the illumination spot.

In contrast to 1D gap solitons, which have a well-defined number of particles and size determined solely by the effective mass and nonlinearity [20], 2D GS can accommodate different number of particles N . The size (diameter) of the GS is expected to depend only weakly on N . The initial increase in the ϕ_{GS} size in figure 3(b) indicates that it also depends on the dimensions of the illumination spot. The weak dependence of ϕ_{GS} on P_L may explain the saturation of ϕ_{GS} (and ℓ) with increasing laser excitation displayed in figure 3. At present we cannot, however, fully discard other saturation mechanisms. One may argue, for instance, that the saturation of ϕ_{GS} arises from energy blue-shift due to inter-particle interactions which displaces the states at \mathbf{k}_p towards the laser energy with increasing particle density, thus reducing the injection efficiency of pump polaritons. The additional experimental results presented in the supplementary materials section show, in fact, that the total emission of GSs excited by a small laser spot exhibits a plateau for laser power densities between 70 and $300 \mu\text{W} \mu\text{m}^{-2}$. The plateau is, however, followed by a second increase in emission intensity for $P_L > 300 \mu\text{W} \mu\text{m}^{-2}$, which is not reflected in the data of figure 3(a). This second increase is probably due to the

fact that the blueshift (which increases continuously with P_L) brings other (folded) dispersion branches in resonance with the laser. Furthermore, injection saturation cannot be invoked to explain the data for the large excitation spot (see figure 3(b)), since here ϕ_{GS} (and ℓ) saturate already at the threshold excitation density, where the blue-shift is at its minimum. We note, however, that particle density may also affect the GS size by shifting their energy levels and screening the acoustic modulation potential. A complete analysis of these effects is beyond the scope of the present study.

The MQSs formed along the $X \rightarrow M$ direction have a symmetry different from the GS states, since they form at hyperbolic points of the dispersion. The effective mass along the $X \rightarrow \Gamma$ direction is negative while the one along $X \rightarrow M$ one is positive (see figure 1(b)). As a result of this anisotropic mass configuration, the type- X modes are expected to be quasi-1D with preferential self-confinement along the $X \rightarrow \Gamma$ direction, in agreement with the k -space images in figure 2 for states with energy close to E_X .

In order to understand the nature of the $M \rightarrow X$ states, theoretical calculations were carried out to determine self-localized solutions of the GPE using a variational method. The method only considers the energetic configuration of the signal state of MQS. Its application for the present non-equilibrium problem is justified by the long MQS coherence time (a few hundred of ps) compared to the photon lifetime in the microcavity (tens of ps). Under these conditions, the MQS properties can be approximated by a mean-field, quasi-static approach [21, 22]. In fact, previous investigations (see [13]) have shown that such procedures deliver results compatible with a full numerical solutions of GPE taking into account the OPO process.

The GPE for interacting particles of mass m_p has the mathematical form of the nonlinear Schrödinger equation and can be expressed as:

$$\hat{H}_{\text{GPE}} = -\frac{1}{2} \frac{\hbar^2}{m_p} \hat{\nabla}^2 + \hat{V}_{\text{SAW}} + g |\hat{\psi}|^2. \quad (1)$$

This equation includes the acoustic potential $V_{\text{SAW}}(x, y) = -\Phi_{\text{SAW}} [\cos(k_{\text{SAW}} x) + \cos(k_{\text{SAW}} y)]$ and a nonlinear term accounting for the repulsive interactions between N particles defined by an inter-particle interaction constant $g = 10 \mu\text{eV} \mu\text{m}^2$. We sought for stationary solutions using an Ansatz wave function for confined MQS modes in a square lattice of the form:

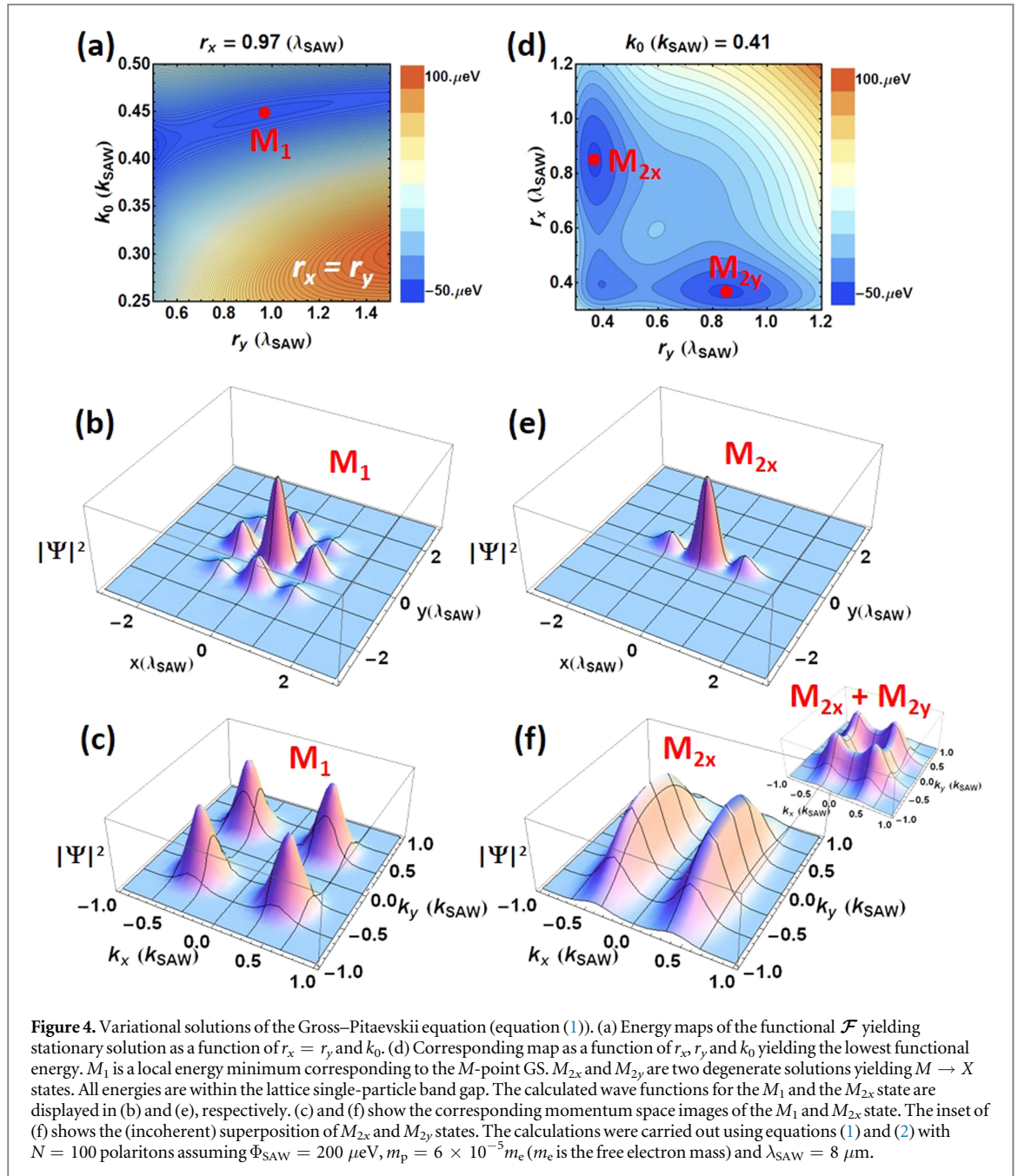
$$\Psi_{\text{Ansatz}}(x, y) = \sqrt{\frac{N}{\pi}} \frac{2 e^{-\left(\frac{x}{r_x}\right)^2 - \left(\frac{y}{r_y}\right)^2}}{\sqrt{r_x r_y (e^{-k_0^2(r_x^2 + r_y^2)} + e^{-k_0^2 r_x^2} + e^{-k_0^2 r_y^2} + 1)}} \cos(k_0 x) \cos(k_0 y). \quad (2)$$

This Ansatz wave function, which yields the particle density, has a Gaussian envelope function and is normalized as $\langle \Psi_{\text{Ansatz}} | \Psi_{\text{Ansatz}} \rangle = N/r_x r_y$. The parameters r_x and r_y define the spatial extensions along the x and y directions, respectively, which are directly related to the characteristic lengths $\ell_{x,y} = \sqrt{2 \ln 2} r_{x,y}$. Finally, the wave vector k_0 defines the oscillation period of the mode.

The numerical solution procedure involves the minimization of the functional $\mathcal{F} = \langle \Psi_{\text{Ansatz}} | \hat{H}_{\text{GPE}} | \Psi_{\text{Ansatz}} \rangle$ with respect to r_x , r_y and k_0 , which yields stationary solutions when $\delta \mathcal{F}(\Psi_{\text{Ansatz}}) = 0$. The fixed values of the number of particles is $N = 100$ in a lattice with periodicity $\lambda_{\text{SAW}} = 8 \mu\text{m}$ and acoustic potential $\Phi_{\text{SAW}} = 200 \mu\text{eV}$. During the minimization, no restrictions at all have been made regarding the values of the parameters r_x , r_y , k_0 . As can be seen in figure 4, our calculations simultaneously yield MQSs at the M - and X -points. The left panel shows solutions of square symmetry obtained by imposing $r_x = r_y$. The energy plot of \mathcal{F} in the $r_x = r_y$ versus k_0 plane of figure 4(a) displays a local minimum M_1 with energy within the single-particle band gap (note that the absolute minimum, which is associated with the Γ state with $k_0 = 0$ and the $r_x, r_y \rightarrow \infty$ lies outside the plot range). The effective wave vector for this mode $k_0 = 0.45 k_{\text{SAW}}$ is close to the one associated with the M point (equal to $k_{\text{SAW}}/2$), thus implying that the phase of the wave function changed by approximately 180° between consecutive periods. This solution is similar to the one determined for the GS states in [13]: it corresponds to a mode with symmetric ℓ lengths of a few SAW periods ($\ell_{x,y} \sim 3 \lambda_{\text{SAW}}$) and M -point symmetry in momentum space, as indicated by the wave function representations in figures 4(b) and (c), respectively.

The variational solutions for the MQSs that form along $X \rightarrow M$ symmetry were calculated by exploring the parameter region with $r_x \neq r_y$ (right panels of figure 4). The functional energy plot (see figure 4(d)) reveals in this case two degenerate modes M_{2x} and M_{2y} with extended characteristic length ℓ along one direction ($\sim 3 \lambda_{\text{SAW}}$) and reduced ℓ ($\sim \lambda_{\text{SAW}}$) along the perpendicular one. The wave function representations of mode M_{2x} in real and momentum space are displayed in figures 4(e) and (f), respectively. The corresponding plots for the M_{2y} modes can be obtained by simply interchanging the x and y (or k_x and k_y) axis.

Objects similar to the MQSs that form along $X \rightarrow M$ symmetry (called ‘in-band’ solitons) have been observed in nonlinear crystals [23]. The fact that the band effective mass is negative in the $X \rightarrow \Gamma$ direction allows them to self-localize in a similar way as the GS wave packet discussed above, conferring them thus a solitonic character. At small number particle or weak interactions, their energy is within the energy band of the



lattice dispersion, but, if the interactions are strong enough, they may also rise within the gap, thus becoming 1D GSs. Our model predicts correctly the existence of these states, and in our experiments we observe a marked blue-shift and flattening of the dispersion along $X \rightarrow M$ (see the k -space spectra in Figure 2), which give some evidence of this kind of behaviour. The in-band to GS transition is however continuous, and its detailed characterization is beyond the scope of the present work. To our best knowledge, however, the present study reports the first observation of MQS with hyperbolic dispersion in a polariton system [18]. Based on these results, we attribute the k -space tomograms in figure 2 with energy E_X to the superposition of M_{2x} and M_{2y} modes excited around the central 2D GS state. In fact, the k -space maps expected from the (incoherent) superposition on M_{2x} and M_{2y} states (see inset figure 4(f)) look very similar to the experimental ones with $X \rightarrow M$ symmetry displayed in figure 2.

A final important question regards the relative stability and spatial separation of the GSs and $X \rightarrow M$ MQSs, in particular, why the latter only form at the flanks for the excitation beam. A possible explanation relies on the fact that the effective mass is negative only along one direction. The latter makes the excitation of M_{2x} and M_{2y} states under homogeneous illumination less probable than for the M_1 states. The situation becomes different in the ring around the central 2D GS, which is subject to a radial energy gradient due to the decaying particle densities and to a highly asymmetric illumination profile. Additionally, this gain region has a ring-shape due to

the depletion of the central part by the GS states. We speculate that the reduction in symmetry in the pump and signal states induces the preferential formation of $X \rightarrow M$ states in this region. We remind the reader that the variational procedure presented above does not take into account energy gradients.

5. Summary and conclusions

We have performed a tomographic study of the formation of MQS in an acoustic square lattice. The study reveals that the MQSs self-organize in a discrete structure, where three concentric modes coexist under excitation by a Gaussian beam. The central mode is a single GS wave packet reported in [13], which robustly forms over a large range of excitation parameters. The energy-filtered reveal that the diameter ϕ_{GS} of the GS emission is very close to the characteristic length ℓ measured from reciprocal space images. While the total emission area ϕ_{PL} of the MQS is also equal to ϕ_{GS} and ℓ for optical excitation close to the threshold, it increases above these values for high excitation intensities. We have shown that the extra emission does not arise from multiple type- M GS states, but rather from multiple MQSs with shorter characteristic length excited at hyperbolic regions (X -points) of the dispersion. The existence of these modes has also been confirmed by a variational solution of the GPE for interacting polaritons in a square lattice.

In conclusion, the present studies provide an insight into the dynamics of polariton MQS in lattices. The latter is relevant for the implementation of polaritonic devices for information processing using more sophisticated entities such as vortex lattice solitons or, in the limit of very short acoustic wavelengths, single polaritons.

Acknowledgments

The authors wish to thank S Fernández-Garrido for fruitful discussions and A Tahraoui, S Rauwerdink, W Seidel, and B Drescher for sample processing. This work was supported by Deutsche Forschungsgemeinschaft grants No. CE 191/2-1 and SA 598/10-1, PROALMEX-DAAD grant No. 57064990 and Consejo Nacional de Ciencia y Tecnología grant No. 207216 for sabbatical leave.

References

- [1] Morsch O and Oberthaler M 2006 Dynamics of Bose–Einstein condensates in optical lattices *Rev. Mod. Phys.* **78** 179
- [2] Bloch I, Dalibard J and Zwerger W 2008 Many-body physics with ultracold gases *Rev. Mod. Phys.* **80** 885
- [3] Greiner M, Mandel O, Esslinger T, Hansch T W and Bloch I 2002 Quantum phase transition from a superfluid to a Mott insulator in a gas of ultracold atoms *Nature* **415** 39–44
- [4] Georgescu I M, Ashhab S and Nori F 2014 Quantum simulation *Rev. Mod. Phys.* **86** 153–85
- [5] Kartashov Y V, Malomed B A and Torner L 2011 Solitons in nonlinear lattices *Rev. Mod. Phys.* **83** 247–305
- [6] Deng H, Haug H and Yamamoto Y 2010 Exciton–polariton Bose–Einstein condensation *Rev. Mod. Phys.* **82** 1489
- [7] Carusotto I and Ciuti C 2013 Quantum fluids of light *Rev. Mod. Phys.* **85** 299–366
- [8] Lai C W *et al* 2007 Coherent zero-state and [pgr]-state in an exciton–polariton condensate array *Nature* **450** 529–32
- [9] Cerda-Méndez E A *et al* 2010 Polariton condensation in dynamic acoustic lattices *Phys. Rev. Lett.* **105** 116402
- [10] Kim N Y *et al* 2011 Dynamical d-wave condensation of exciton–polaritons in a two-dimensional square-lattice potential *Nat. Phys.* **7** 681–6
- [11] Gorbach A V, Malomed B A and Skryabin D V 2009 Gap polariton solitons *Phys. Lett. A* **373** 3024–7
- [12] Tanese D *et al* 2013 Polariton condensation in solitonic gap states in a one-dimensional periodic potential *Nat. Commun.* **4** 1749
- [13] Cerda-Méndez E A *et al* 2013 Exciton–polariton gap solitons in two-dimensional lattices *Phys. Rev. Lett.* **111** 146401
- [14] Kim N Y *et al* 2013 Exciton–polariton condensates near the Dirac point in a triangular lattice *New J. Phys.* **15** 035032
- [15] Jacqmin T *et al* 2014 Direct observation of Dirac cones and a flatband in a honeycomb lattice for polaritons *Phys. Rev. Lett.* **112** 116402
- [16] Cerda-Méndez E A *et al* 2010 One dimensional confinement of microcavity polaritons using non-piezoelectric surface acoustic waves *Physica E* **42** 2548–51
- [17] Nardin G *et al* 2009 Probability density optical tomography of confined quasiparticles in a semiconductor microcavity *Appl. Phys. Lett.* **94** 181103
- [18] Cerda-Méndez E A *et al* 2012 Dynamic exciton–polariton macroscopic coherent phases in a tunable dot lattice *Phys. Rev. B* **86** 100301
- [19] Krizhanovskii D N *et al* 2013 Effect of polariton–polariton interactions on the excitation spectrum of a nonequilibrium condensate in a periodic potential *Phys. Rev. B* **87** 155423
- [20] Eiermann B *et al* 2004 Bright Bose–Einstein gap solitons of atoms with repulsive interaction *Phys. Rev. Lett.* **92** 230401
- [21] Pethick C J and Smith H 2002 *Bose–Einstein Condensation in Dilute Gases* (Cambridge: Cambridge University Press)
- [22] Pitaevskii L P and Stringari S 2003 *Bose–Einstein Condensation* (Oxford: Clarendon)
- [23] Wang X, Chen Z, Wang J and Yang J 2007 Observation of in-band lattice solitons *Phys. Rev. Lett.* **99** 243901